Extreme Mechanics Letters 73 (2024) 102245

Contents lists available at ScienceDirect

Extreme Mechanics Letters

journal homepage: www.elsevier.com/locate/eml

Orientation-dependent deformation and failure of micropillar shape memory ceramics: A 3D phase-field study

Amirreza Lotfolahpour, Mohsen Asle Zaeem *

Department of Mechanical Engineering, Colorado School of Mines, 1500 Illinois street, Golden, CO 80401, USA

ARTICLE INFO

Keywords:
Shape memory ceramics
Phase-field modeling
Martensitic phase transformation
Fracture
Crystal plasticity

ABSTRACT

Some microscopic samples of zirconia-based shape memory ceramics (SMCs) have shown full martensitic phase transformation (MPT) over multiple loading cycles without cracking. However, the occurrence of MPT is strongly influenced by grain orientation. Depending on the specific grain orientation relative to the loading direction, alternative mechanisms such as plastic slip and fracture may emerge. This study introduces a phase-field (PF) based framework that integrates a PF-MPT model, a PF fracture model, and a crystal viscoplasticity model to investigate the effects of grain orientation on MPT, plastic slip, and fracture mechanisms in SMC micropillars. Single crystal micropillars are created to distinguish the orientations that facilitate each mechanism. A wide range of grain orientations are found to predominantly exhibit MPT. Micropillars with grain orientations close to the (100) and (001) directions primarily experience fracture, with minimal plastic slip. Additionally, samples oriented along the (110) direction show a significant amount of plastic slip. A pole figure is constructed to elucidate the interplay between MPT, cracking, and plastic slip under compressive loading conditions. This research provides valuable insights into the intricate behavior of SMCs under different loading scenarios, crucial for optimizing their performance in practical applications.

1. Introduction

Zirconia-based SMCs are intelligent materials known for their capacity of demonstrating either superelasticity or shape memory effect as a result of MPT. MPT arises from phase change mainly between tetragonal (*T*) and monoclinic (*M*) phases. The shape change induced by MPT is large and due to the inherent brittleness of these ceramics, they are often unable to accommodate such significant transformation expansions. This is the main reason for their low fracture toughness and short cyclic life. Multiple experimental studies on microscopic samples of these ceramics have consistently highlighted grain boundaries (GBs) as critical sites for crack initiation [1–3]. These investigations have demonstrated that by reducing the number of grains and consequently minimizing the presence of GBs and even generating single crystal samples, these ceramics can undergo complete MPT over numbers of loading cycles before experiencing fracture. For example, Lai et al. [1] produced micropillars with low number of grains and they observed that some samples can handle up to 55 cycles before they fractured. In addition, experimental studies have identified plastic slips as one primary irreversible mechanism in these ceramics. In a different study, Du et al. [2] showed that single crystal spherical samples of 16 mol% Ce-ZrO_2 are able to handle up to about 110 cycles before they showed fracture. Zeng et al. [3] observed that depending on the crystal orientation in single crystal micropillars, these ceramics can exhibit MPT, plastic slip, fracture, or a combination of these three mechanisms.

MPT, plastic slip, and fracture are highly dependent on microstructural features [3], and comprehensively understanding how these features influence the interplay between these mechanisms can be challenging, if not impossible, solely through experimental methods. In this case, numerical studies can be a reliable alternative to experiments. There have been a few atomistic simulation studies which investigated the crystal orientation [4] and grain boundary [5,6] effects on superelastic and shape memory behaviors [7] in zirconia-based nanopillars. These studies, although valuable in providing some fundamental understanding of mechanisms and behaviors in the nanoscale, due to their time and length scale limits are unbale to compare with the actual experiments. At the microscale, the PF method has emerged as a powerful approach for modeling both MPT and fracture. The first PF method to model the transformation from *T* to *M* phase observed in zirconia-based SMCs was developed more than a decade ago [8]. The model could

* Corresponding author.
E-mail address: zaeem@mines.edu (M. Asle Zaeem).

https://doi.org/10.1016/j.eml.2024.102245
Received 16 June 2024; Received in revised form 19 September 2024; Accepted 10 October 2024
Available online 11 October 2024

successfully capture the crystal alternation between the two phases and accurately predicted the experimentally observed microstructures. Similar models were used later on to study transformation toughening [9] and shape memory behaviors [10] in SMCs. The PF method has also been utilized to model the interaction between MPT and cracking in SMCs [11–16]. For instance, Moshkelgosha and Mamivand conducted studies on fracture propagation in both single crystal [13] and polycrystalline [14] zirconia-based SMCs using the PF method. They employed stress-controlled loading conditions. In a separate investigation by the same authors [15], they explored phase transformation and fracture in a three-dimensional single crystal SMC, observing the initiation and propagation of MPT from the crack tip. They predicted crack deflection due to MPT, consistent with experimental reports. Notably, none of these studies reported an ultimate stress or final stress drop in their stress-strain curves, primarily because of applying stress-controlled loading conditions. Additionally, these studies focused only on shape memory effect behavior and none studied the superelastic behavior. Furthermore, these models did not include plasticity, therefore they were not able to study the interplay between MPT, fracture, and plastic slip.

Recently, Lotfolahpour et al. [16] proposed a PF model to investigate the interaction between MPT and cracking in the SE regime. They addressed a common issue of the most PF-MPT models that underestimate the elastic modulus. They successfully established an ultimate strength for the material under investigation by applying displacement-controlled loadings. Their work studied the effects of grain orientation on MPT and crack path and captured reverse MPT behind the crack tip. In another research, Cisse and Asle Zaeem [17], coupled the PF-MPT model with a Von Mises based plasticity model to study the interaction between MPT and plasticity in SMCs under monolithic loading conditions. They identified GBs as critical sites with the highest plastic strain. In addition, they observed that plastic deformation impedes MPT and compromises the functionality of SMCs. There are additional studies that focus on coupling PF-MPT with plasticity, either general plasticity or crystal plasticity models, to examine the interaction between MPT and plastic deformation in shape memory materials, with a primary focus on NiTi [18–21]. However, none of these previous studies have investigated MPT, plasticity, and fracture simultaneously, and consequently, they have not been able to establish a comprehensive understanding of the interaction between these mechanisms. In this study, for the first time, we integrate MPT, plastic slip, and fracture models to investigate the interplay between these mechanisms in 3D micropillars. We utilize the PF method to model both MPT and fracture, while adopting a crystal viscoplasticity model to accurately represent plastic slip behavior in SMCs crystals. The aim is to predict the orientation-dependent deformation and failure of micropillar SMCs. To better present our findings, we illustrate the results in a pole figure comparable to those created by micropillar experiments of SMCs.

2. Mathematical formulation

In this section, we first describe the integration of the elasticity, PF-MPT and PF-fracture models. Then, we add plastic strains from slip systems to the inelastic strain expression and discuss the calculation of the plastic strains based on a crystal viscoplasticity model. We start the formulation by expressing the total energy of the system as:

$$F_{\text{tot}}(u_i,\quad \eta_1,\eta_2,\quad \ldots,\quad \eta_m) = F_{\text{el}} + F_{\text{ch}} + F_{\text{gd}} + F_{\text{fr}} \tag{1}$$

where F_{el} is the elastic strain energy, F_{ch} is the chemical free energy, F_{gd} is the gradient energy of the tetragonal-monoclinic or monoclinic-monoclinic interfaces, and F_{fr} is the fracture energy. These energies are explained in detail in the following.

- *Elastic strain energy* (F_{el}):

F_{el} can be written as:

$$F_{\text{el}}(u_i) = \int_V \frac{1}{2} g(\phi) C_{ijkl} \varepsilon_{kl}^{\text{el}} \varepsilon_{ij}^{\text{el}} dV, \tag{2}$$

where u_i is the displacement, C_{ijkl} is the elastic tensor, and $g(\phi)$ is the degradation function to account for the effects of fracture on the elastic energy. It should be noted we use $g(\phi) = (1-\phi)^2$ in this work, which is one of the widely used degradation functions. In addition, $\varepsilon_{ij}^{\text{el}}$ is the elastic strain which is defined as the difference between the total strain ($\varepsilon_{ij}^{\text{tot}}$), transformation strain ($\varepsilon_{ij}^{\text{tr}}$), and plastic strain ($\varepsilon_{ij}^{\text{pl}}$):

$$\varepsilon_{ij}^{\text{el}} = \varepsilon_{ij}^{\text{tot}} - \varepsilon_{ij}^{\text{tr}} - \varepsilon_{ij}^{\text{pl}}. \tag{3}$$

The calculation of plastic strain is explained later in this section. Considering a linear relation between PF order parameters (η_p) and strains [16,22–24], $\varepsilon_{ij}^{\text{tr}}$ is defined as:

$$\varepsilon_{ij}^{\text{tr}} = \quad \sum_{p=1}^{m} \varepsilon_{ij}^{00}(p)\eta_p, \tag{4}$$

where ε_{ij}^{00} is the stress-free strain tensor which represents the change in microstructure between parent and product phases [17]. It should be noted that η_p takes the value of unity in the monoclinic phase and zero in the tetragonal phase, and m is the number of monoclinic variants.

The small strain assumption is considered and is defined as:

$$\varepsilon_{ij}^{\text{tot}} = \frac{1}{2} \quad \left(u_{i,j} + u_{j,i}\right). \tag{5}$$

The difference between elastic constants in tetragonal and monoclinic phase is represented by the following linear relation [17]:

$$C_{ijkl}(\eta_1, \quad \eta_2, \ldots, \quad \eta_m) = \quad C_{ijkl}^{T} + \quad \sum_{p=1}^{m} \eta_p \left(C_{ijkl}^{M} - C_{ijkl}^{T}\right), \tag{6}$$

where C_{ijkl}^{T} and C_{ijkl}^{M} are elastic constants of the tetragonal and monoclinic phase, respectively. The elastic energy defined in Eq. (2) is based on the Hooke's law, therefore the stress tensor is related to the elastic strain tensor through the following equation:

$$\sigma_{ij}\left(u_i, \eta_p\right) = C_{ijkl}(\eta_1, \quad \eta_2, \ldots, \quad \eta_m)\varepsilon_{kl}^{\text{el}}. \tag{7}$$

- *Chemical free energy* (F_{ch}):

F_{ch} determines the system's energy dissipation due to MPT. The 2–3–4 or 2–4–6 Landau polynomials defined in terms of order parameters are the most common types of F_{ch} [25]. However, these chemical energies can underestimate the elastic response in the beginning of the stress-strain curve. Lotfolahpour et al. [16] proposed a modification to the 2–3–4 polynomial to address the elastic modulus underestimation, which is applied in this work as well:

$$F_{\text{ch}}(\eta_1, \eta_2, \ldots, \eta_m) = \int_V |\Delta G| \left(a \sum_{p=1}^{m} \eta_p^2 - b \sum_{p=1}^{m} \eta_p^3 + c \left(\sum_{p=1}^{m} \eta_p^2 \right)^2 + d \sum_{p=1}^{m} |\eta_p|^n \right) dV \tag{8}$$

$1 < n \ll 2,$

where ΔG is the chemical driving force and is the difference in the specific F_{ch} between the parent (tetragonal) and the product (monoclinic). The following equation can be used to calculate ΔG for 3Y-STZ at different temperatures [17,26]:

$$\Delta G(T\rightarrow M) = -6159.18 + 6.98\mathrm{T} \tag{9}$$

where the energy is in Jmol^{-1}(or Jm^{-3}) and the temperature (T) is in Kelvin (K). In addition, a, b, c, d, and n are coefficients that should be chosen in a way that maintain the value of the interfacial energy within the physical reasonable range [16] and at $\eta_p = 1$ result in $F_{\mathrm{ch}} = \Delta G(T\rightarrow M)$.

- *Gradient free energy* (F_{gd}):

F_{gd} represents the interfacial energy between the tetragonal and monoclinic phases and ensures a smooth transition of the PF order parameters between different phases. It is expressed as:

$$F_{\mathrm{gd}}(\eta_1, \eta_2, \quad \ldots, \eta_m) = \int_V \frac{B_{ij}}{2} \sum_{p=1}^{m} \nabla_i \eta_p \nabla_j \eta_p dV, \tag{10}$$

where ∇ is the gradient operator and B_{ij} is gradient energy tensor. We assume that the gradient energy coefficient is isotropic ($B_{ij} = B\delta_{ij}$) [17]. Therefore the Eq. (10) becomes:

$$F_{\mathrm{gd}}(\eta_1, \eta_2, \quad \ldots, \eta_m) = \int_V \frac{B}{2} \sum_{p=1}^{m} (\nabla \eta_p)^2 dV. \tag{11}$$

- *Fracture energy* (F_{fr}):

$\mathrm{Jmol}^{-1}\mathrm{Jm}^{-3}\mathrm{T}abcd n\eta_p = 1F_{\mathrm{ch}} = \Delta G(T\rightarrow M)F_{\mathrm{fr}}$ presents the fracture energy in the system and is defined as [27–29]:

$$F_{\mathrm{fr}}(\phi) = \int_V G_c \left(\frac{\phi^2}{2k} + \frac{k}{2} |\nabla \phi|^2 \right) dV, \tag{12}$$

where G_c is the fracture surface energy in Griffith's theory, and k is a positive regularization parameter with the dimension of length to regulate the width of the crack PF. ϕ is the PF fracture order parameter that takes value of unity in cracked regions and zero in intact regions. In this paper, we use the method proposed by Miehe et al. [30] to ensure irreversibility of crack (crack healing prevention):

$$F_{\mathrm{el}}(u_i, t) = \max F_{\mathrm{el}}(u_i, s), \quad s \in [0, t]. \tag{13}$$

2.1. Governing equations of MPT and fracture

The evolution of both MPT and PF fracture are obtained by Ginzburg-Landau equation [31]. This equation relates the rate of each order parameter to the variational derivative of total free energy with respect to the same order parameter. Using Ginzburg-Landau equation for MPT yields the following evolution equation for PF order parameters:

$$\frac{\partial \eta_p}{\partial t} = L\left(\frac{\delta F_{\mathrm{tot}}}{\delta \eta_p}\right) = \quad L \quad \left(\frac{\delta F_{\mathrm{el}}}{\delta \eta_p} + \frac{\delta F_{\mathrm{ch}}}{\delta \eta_p} + \frac{\delta F_{\mathrm{gd}}}{\delta \eta_p} + \frac{\delta F_{\mathrm{fr}}}{\delta \eta_p}\right), \tag{14}$$

where L is the kinetic coefficient. The extended equations are presented in appendix A.

In addition, using the Ginzburg-Landau equation for PF fracture leads to:

$$\frac{\partial \phi}{\partial t} = M\left(\frac{\delta F_{\mathrm{tot}}}{\delta \phi}\right) = \quad M \quad \left(\frac{\delta F_{\mathrm{el}}}{\delta \phi} + \frac{\delta F_{\mathrm{ch}}}{\delta \phi} + \frac{\delta F_{\mathrm{gd}}}{\delta \phi} + \frac{\delta F_{\mathrm{fr}}}{\delta \phi}\right), \tag{15}$$

where M is called the fracture mobility coefficient. More details are provided in appendix A.

In addition, by neglecting the body forces, the equilibrium equations become:

$$\mathrm{div}\boldsymbol{\sigma}(u_i, \phi) = 0. \tag{16}$$

2.2. Crystal viscoplasticity

Atomistic simulations [4] and experimental observations [3] have established plastic slip as the predominant irreversible deformation mechanism in single crystal zirconia-based SMCs oriented in particular directions. To incorporate plastic slip in our formulation, we employ crystal viscoplasticity. Slip systems are defined by two vectors: normal vector of the slip plane ($\vec{p}$) and the slip direction vector ($\vec{d}$). Plastic strain tensor of the nth slip system is expressed as [32]:

$$\varepsilon_{ij}^{\mathrm{pl}} = \sum_{n=1}^{N} \dot{\gamma}_n P_{n_{ij}} \tag{17}$$

where N is the total number of slip systems, $\dot{\gamma}_n$ is the plastic slip evolution rate, and P_{ij} are the components of the orientation tensor ($\boldsymbol{P}_n$), also knowns as symmetrized Schmid tensor, of the nth slip system and is calculated as:

$$\boldsymbol{P}_n = \frac{1}{2}(\vec{p_n} \otimes \vec{d_n} + \vec{d_n} \otimes \vec{p_n}) \tag{18}$$

In addition, the accumulated plastic slip and the magnitude of plastic slip at time t are defined by [32] following equations respectively:

$$\dot{\gamma} = \sum_{n=1}^{N} |\dot{\gamma}_n| \tag{19}$$

$$|\gamma| = \int_0^t \dot{\gamma} dt \tag{20}$$

A slip system becomes active when the resolved shear stress on the slip plane and in the slip direction reaches a critical or yield stress threshold (τ_{cr}). The resolved shear stress in the slip direction, a scalar quantity, is computed as follows [33]:

$$\tau_n = \boldsymbol{\sigma}(u_i, \phi) \cdot \boldsymbol{P}_n \tag{21}$$

There are various flow rules to calculate the $\dot{\gamma}_n$. In this study, we use the following relation which is based on the Chaboche-type potential [32]:

$$\dot{\gamma}_n = \vartheta \ \mathrm{sgn}(\tau_n) \left\langle \frac{|\tau_n| - \tau_{cr_n}}{\tau_{D_n}} \right\rangle_+^{m_n} \tag{22}$$

where ϑ is the viscosity coefficient, m and τ_D are model constants, and the Macaulay brackets is defined as $\langle * \rangle_+ = \max(0, *)$. In addition, τ_{cr_n} is a function of $|\gamma|$ and is defined to take the following form:

$$\begin{cases} \tau_{cr_n} = \sigma_{yo_n} + H_n |\gamma| \xi_n & \text{if } \tau_{cr_n} > \sigma_{yo_{\min_n}} \\ \tau_{cr_n} = \sigma_{yo_{\min_n}} & \text{if } \tau_{cr_n} \leq \sigma_{yo_{\min_n}} \end{cases} \tag{23}$$

where σ_{yo_n} is the initial yield, H_n is the hardening modulus, and $\sigma_{yo_{\min_n}}$ is the lowest possible yield stress of nth slip system.

2.3. Solution scheme and boundary conditions

The governing equations presented in the previous section are solved in a finite element framework using the solid mechanics and mathematics modulus of COMSOL Multiphysics. All simulations are under load-controlled loading conditions unless otherwise stated. The boundary conditions and sample dimensions are shown in Fig. 1. For all models, quadrilateral 3D elements are generated by the swept mesh algorithm feature in COMSOL. A mesh study was conducted where we

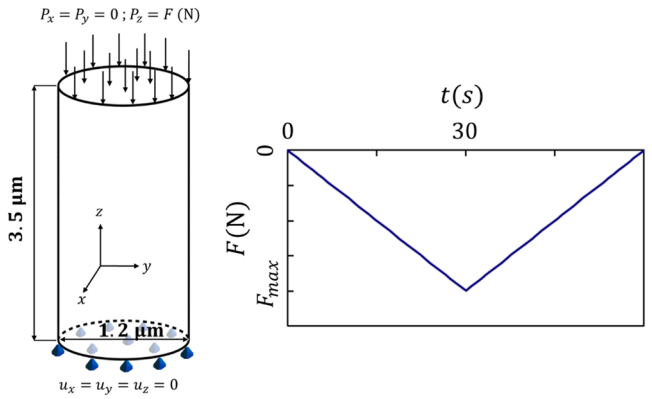

Fig. 1. Micropillar dimensions and boundary conditions.

found that a mesh size of 0.07 μm (or 18200 quadrilateral elements in the domain) were sufficient to resolve the interface of different phases and PF fracture profile, and a smaller mech size does not provide a noticeably different result. The displacements are solved using the Solid Mechanics module. The crack PF and Martensite PF are solved using the General Form PDE module of COMSOL. In addition, the crystal plasticity strains are calculated using the Domain ODEs module. The staggered scheme [34] is used to solve the governing equations and the time step of 0.05s is used for all simulations. In the staggered method, the governing equations are solved sequentially rather than simultaneously. During each iteration, one equation is solved while the others remain fixed. The system alternates between equations, updating each field in turn. This iterative process continues until convergence is achieved, with the error in each equation minimized to an acceptable level. By updating one physical field at a time, the staggered method simplifies the solution of complex multiphysics problems, making the process more efficient and manageable, especially when direct coupling is computationally demanding.

2.4. Material properties and model parameters

3Y-STZ (3 mol% yttria-stabilized tetragonal zirconia), which is a SMC [35,36], is the material of study in this work. The equilibrium temperature of 3Y-STZ is reported to be ~883 K [17]. We consider the temperature of the system is constant and equal to 820 K and we use this temperature to calculate ΔG in Eq. (9) which yields $\Delta G = -433$ Jmol^{-1} (-20×10^6 Jm^{-3}). It is worth noting that the considered temperature is lower than the equilibrium temperature, therefore, the system is in SME regime (full strain recovery does not occur after unloading). Eq. (24) and Eq. (25) show the stiffness tensor of tetragonal and monoclinic phases, respectively [37,38]. In addition, 3Y-STZ has 12 different M variants, and the stress-free strain tensor of each variant is expressed in appendix A [15].

$$\boldsymbol{C}^{T}_{ijkl} = \begin{bmatrix} 361 & 100 & 62 & 0 & 0 & 0 \\ 100 & 361 & 62 & 0 & 0 & 0 \\ 62 & 62 & 264 & 0 & 0 & 0 \\ 0 & 0 & 0 & 59 & 0 & 0 \\ 0 & 0 & 0 & 0 & 59 & 0 \\ 0 & 0 & 0 & 0 & 0 & 64 \end{bmatrix} \text{GPa}, \tag{24}$$

Table 1
Model parameters.

Parameters	Values
a, b, c, d, and n	2.15, 11.95, 7.5, 1.25, and 1.1 [17]
$\sigma_{y0_n}, \sigma_{yo_{min_n}}$, H_n, ξ_n, τ_{Dn}, and m_n	0.550 GPa, 0.275 GPa, −150 GPa, 1, 1, and 1
B	1×10^{-6} Jm^{-1}
L	1×10^{-9} Pa^{-1}s^{-1} [16]
M	$1\ \frac{m^3}{Js}$ [16]
ϑ	1×10^{4} Pa^{-1}s^{-1}
G_c, k	200 Nm^{-1} [39], 0.15μm

$$\boldsymbol{C}^{M}_{ijkl} = \begin{bmatrix} 327 & 142 & 55 & 0 & 0 & -21 \\ 142 & 408 & 196 & 0 & 0 & 31 \\ 55 & 196 & 258 & 0 & 0 & -18 \\ 0 & 0 & 0 & 100 & -23 & 0 \\ 0 & 0 & 0 & -23 & 81 & 0 \\ -21 & 31 & -18 & 0 & 0 & 126 \end{bmatrix} \text{GPa}. \tag{25}$$

Table 1 shows the model parameters used in the simulations. a, b, c, d, and n are calculated in a way that the F_{ch} plot is a double-well [17] and the value of F_{ch} is equal to -20×10^6 Jm^{-3} at $\eta_p = 1$. Plastic slip, similar to MPT, forms localized small bands. Incorporating stress softening into the yield stress is crucial for accurately modeling this phenomenon, which necessitates selecting a negative value for the hardening coefficient H_n [40]. The chosen value is notably large and negative, a decision informed by molecular dynamics (MD) findings that report a sharp decline in the stress-strain curve upon slip initiation [41]. In addition, it is important to note that the yield stress never reaches zero or becomes negative, after slip initiation. Consequently, we must establish a minimum yield stress ($\sigma_{yo_{min_n}}$) to account for this behavior. Based on the observed trend in MD simulations, we set $\sigma_{yo_{min_n}}$ to be 50 % of the initial slip yield stress [41]. Also, the approach to find σ_{y0_n} value is discussed in later sections. We chose $B = 1\times10^{-6}\frac{J}{m}$ which gives a reasonable interface thickness between different phases and choosing a smaller value does not affect the results noticeably. We considered the family of {110}<110> as the slip systems of the tetragonal phase [42]. This system encompasses four distinct slip systems, therefore N in Eq. (17) and Eq. (19) is 4. In addition, the Euler angles of the studied micropillars are given in Table 2. It is important to highlight that the orientation of (100) indicates alignment of the a-axis, b-axis, and c-axis of the tetragonal phase with the z-axis, y-axis, and x-axis of the global coordinate system, respectively (Fig. 1), while an orientation of (001) denotes alignment of the a-axis, b-axis, and c-axis of the tetragonal phase with the x-axis, y-axis, and z-axis of the global coordinate system, respectively.

Table 2
Pillar IDs and orientations.

Pillar ID	Euler Angles (in degrees)		
	E1	E2	E3
p1	0	0	0
p2	190	45	230
p3	285	45	320
p5	300	60	350
p6	30	75	340
p7	0	90	45
p8	0	90	0
p9	68	104	305
p10	245	35	200
p11	265	63	16

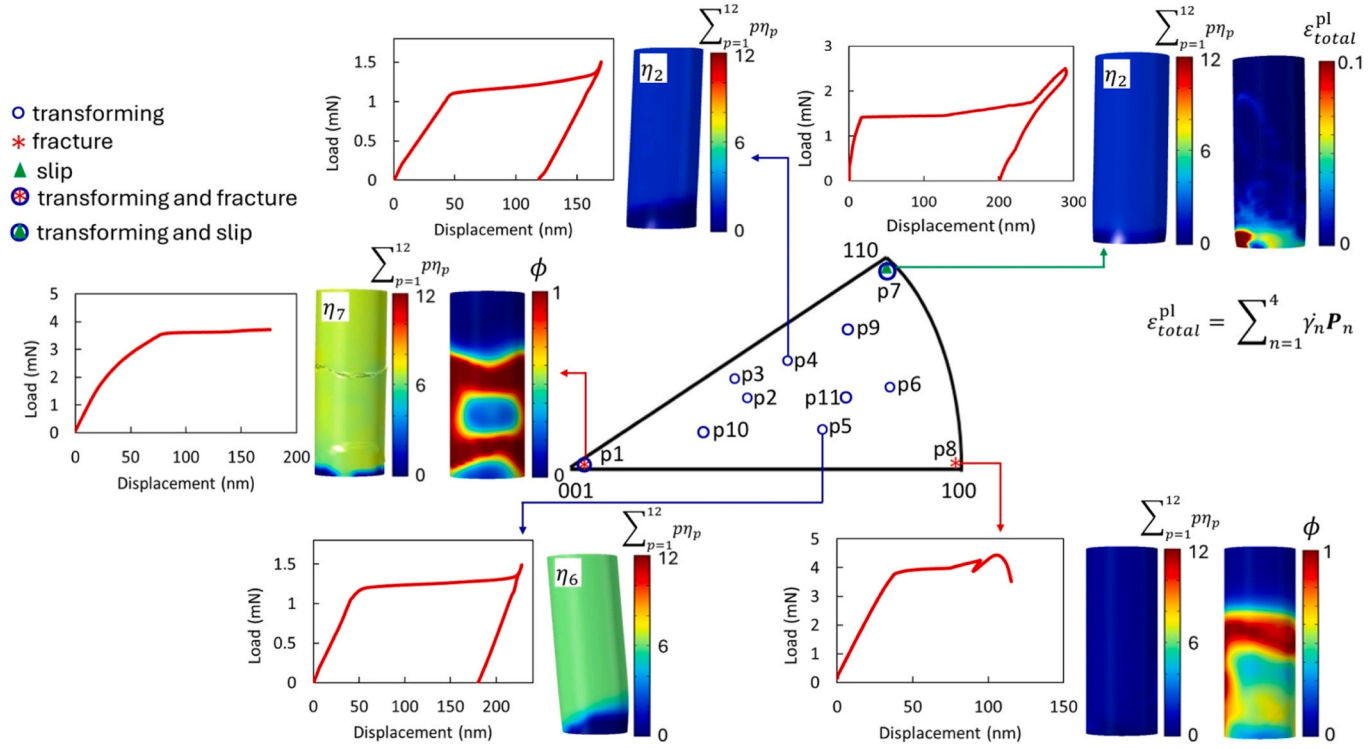

Fig. 2. Pole figure presenting the effects of grain orientation on the interplay between MPT, cracking, and slip in micropillars.

3. Results and discussion

We investigated 11 grain orientations, as detailed in Table 2. To visually represent our findings, we constructed a pole figure with three vertices corresponding to orientations of (100), (110), and (001) as shown in Fig. 2. To differentiate between MPT, slip, and crack, we followed a systematic approach. Initially, a load ranging between 1.5mN to 2mN was applied, and simulations were run for one cycle. If MPT occurred, we classified the pillar as a transforming pillar. It is worth noting that there are no initial monoclinic seeds to trigger MPT, and the occurrence of MPT depends on grain orientation, which will be discussed later. In cases where MPT did not occur, we increased the load to approximately 3mN and observed the results after one cycle. If plastic slip was observed, we designated the pillar accordingly. And, if plastic slip was not observed, we further increased the load to approximately 5mN or higher until cracking was observed. This step-by-step process allowed us to categorize the behavior of each pillar accurately.

Fig. 2 illustrates that a broad range of tested pillars exhibit full MPT. However, pillar p8 displays fracture with minimal amount of MPT or slipping. In pillar p1, a combination of MPT and fracture is observed with a minor plastic slip. In this pillar, MPT initiates at a higher load, explaining the extended plateau before complete fracture development.

Furthermore, pillar p7 demonstrates a considerable amount of plastic slip and a very small amount of MPT. Our findings highlight that the slip systems characterized by these normal vectors of the slip plane ($\vec{p}$) and the slip direction vectors ($\vec{d}$) $\vec{p}$ = <110> and $\vec{d}$ = <110> and $\vec{p}$ = <1$\bar{1}$0> and $\vec{d}$ = <110> exhibit the highest accumulation of plastic slip among all the considered slip systems. The plastic slip is particularly pronounced at the bottom edge of the pillar. This can be attributed to the fully fixed boundary conditions, which induce high stress concentrations, consequently leading to significant plastic deformation at this region. However, it is worth noting that plastic slip also occurs within the middle section of the pillar, as depicted in Fig. 2. It is worth mentioning that in an experimental report, pillars with similar grain orientations were also observed to exhibit only plastic slip [3]. The pole figure presented in Fig. 2, agrees well with a similar experimental test conducted on zirconia-based SMCs [3]. The discrepancy in MPT start load and residual displacement between p7 in this study and the experimental data could be due to the variations in the mechanical properties of the materials under examination. While we utilized properties of 3-YSZ, the material in [3] was $2Y_2O_3$-$5TiO_2$-ZrO_2 (mol%).

In addition, similar to experimental observations [3], our simulations revealed that in pillars exhibiting MPT, only two monoclinic variants out of the 12 possible variants from; specifically, variant 2 (η_2) and variant 6 (η_6), with a predominant occurrence of η_2. This observation can be explained based on the deformation conditions described by its stress-free strain, ε^{00}_{ij} (2). A deformation exerting contraction along the c-axis and expansion along the a-axis and b-axis of the tetragonal crystal structure favors the formation of η_2. This deformation pattern aligns with the effects induced by a compressive load applied along the z-axis. Formation of a monoclinic variant depends on different factors such as grain orientation, loading direction, and boundary conditions, making it a complex and unpredictable phenomenon.

Fig. 3 depicts the load-displacement plots of selected pillars with full MPT. From this figure, it can be deduced that grain orientation

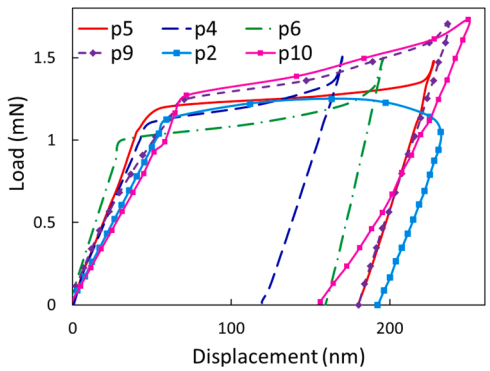

Fig. 3. Load-displacement curve for selected pillars with full MPT.

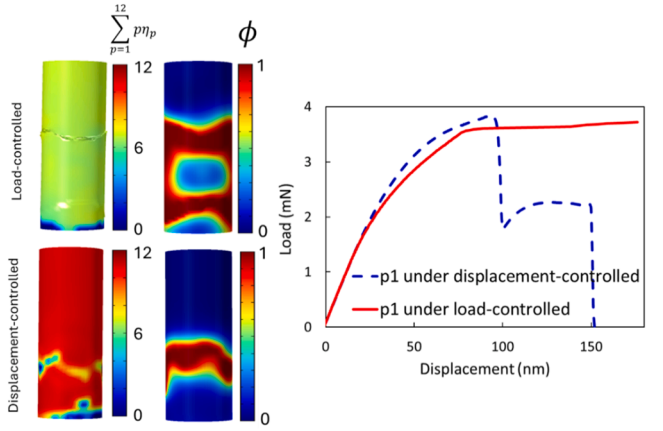

Fig. 4. The crack path, MPT, and mechanical response of p1 under load-controlled and displacement-controlled loading conditions.

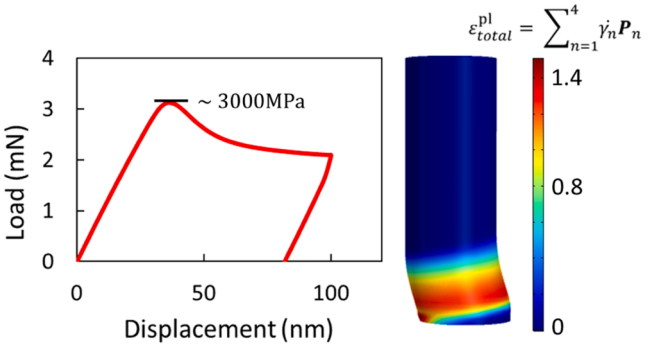

Fig. 5. Slip band formation and load-displacement curve for the micropillar p7 with $\sigma_{y0_n} = 550$ MPa and no MPT.

significantly impacts the elastic modulus in both loading and unloading paths, the critical stress for MPT initiation, and the duration of the plateau. Based on Fig. 3, the critical MPT load (MPT start load) ranges from 0.9 mN (790 MPa) to 1.3 mN (1150 MPa). In addition, the residual displacement is also highly dependent on the grain orientation and ranges from 105 nm (3 % strain) to 190 nm (5.4 % strain).

It is important to note that simulations featuring fracture do not exhibit a final drop and diverge once the crack is fully developed, and this is due to the applied force-controlled loading condition. To observe the ultimate strength and achieve a final drop in the stress-strain curve, a displacement-controlled loading must be applied [16]. To obtain a final drop and establish an ultimate strength, displacement-controlled loading was applied to pillar p1, and the outcomes are presented in Fig. 4.

In Fig. 4, after the first drop in load, another plateau is observed. This is due to the MPT occurrence after crack initiation. This observation explains transformation toughening [9]. In other words, when crack initiates, since stress becomes very high in front of the crack tip(s), MPT triggers and becomes a source of energy dissipation in addition to cracking. The energy dissipation due to MPT slows down the crack propagation. This phenomenon reflects as a plateau or strain hardening in the load-displacement plot. This result is also consistent with MD observations on single crystal 3-YSZ [41]. Furthermore, the distinction in the nature of these two boundary conditions leads to differences in the crack path. While load-controlled simulations exhibit the occurrence of η_7 in displacement-controlled conditions, η_{11} emerges as the only monoclinic phase. This observation can be explained by recognizing that cracks significantly affect the stress distribution within the domain, ultimately affecting the occurrence of different monoclinic variants. Therefore, variations in stress distribution resulting from different crack paths can lead to the occurrence of different monoclinic variants in the material.

3.1. Identification of σ_{y0_n} in the crystal viscoplasticity model

The grain orientation of (110) (or Euler angles of (0°,90°,45°)) yields the highest resolved shear in the slip system of {110}<110>, as the slip direction is closely aligned with the loading direction. To determine the critical resolved shear stress (σ_{y0_n}), we first selected the average plastic yield stress to be 3 GPa [17]. To generate this average stress, a load of 3.4 mN was applied to the micropillar with the radius of 1.2μm. The load was applied to the micropillar p7, and the values for σ_{y0_n} was decreased from 3000 MPa until a slip band was observed. Throughout this process, the objective was to identify the maximum values of σ_{y0_n} that induce the plastic slip, therefore the MPT function is turned off. The critical value of σ_{y0_n} was determined to be around 550 MPa. Fig. 5 depicts the slip band and the load-displacement curve obtained during the identification of σ_{y0_n}. This figure shows that plastic slip localizes to a small band similar to the experimental observations. Furthermore, once slip band forms, the viscosity coefficient (ϑ) influences the deformation and the residual displacement. In Fig. 5, the residual displacement falls within a reasonable and acceptable range, indicating that the value selected for ϑ is suitable.

4. Conclusion

We presented a 3D numerical framework integrating PF-MPT, PF-fracture, and crystal viscoplasticity models to investigate the effects of grain orientation on the interplay of mechanisms of MPT, fracture, and plastic slip in deformation of SMCs under compressive loading conditions.

Our findings revealed that single crystal 3-YSZ micropillars exhibit complete MPT for a wide range of crystal orientations without experiencing irreversible mechanisms of fracture or plastic slip. We observed that the initiation load for MPT ranges between 0.9 mN (790 MPa) to 1.3 mN (1150 MPa) which is in good agreement with experimental data. Moreover, when the pillar's a-axis aligns with the loading direction (z-axis of the global coordinate), fracture emerged as the predominant mechanism, while both MPT and slip occurred minimally.

For the micropillar with the (001) orientation, we observe a combination of both MPT and fracture mechanisms. In the simulation performed under displacement-controlled loading condition, we observed that fracture initiated first in this pillar, followed by the occurrence of MPT. The MPT induced a transformation toughening effect before the pillar experienced complete cracking. Such complex phenomena are challenging, if not impossible, to fully capture through experiments alone. Additionally, this outcome shows the necessity of employing displacement-controlled loading for simulating fracture, capturing the complete process of crack propagation, and establishing the ultimate strength of materials. Unlike load-controlled loading, displacement-controlled loading enables a more comprehensive understanding of fracture mechanisms and facilitates the observation of the entire crack propagation process, which could involve other mechanisms, such as transformation toughening in the case of superplastic or shape memory materials.

For micropillars oriented along the (110) direction, we observed a significant amount of plastic slip and a small amount of MPT. Our model predicted that the plastic slip accumulates predominantly on the slip systems with a normal vector $\vec{p} = <110>$ and along the slip direction of $\vec{d} = <110>$ as well as $\vec{p} = <1\bar{1}0>$ and along $\vec{d} = <110>$. While other slip systems may also be activated, the amount of plastic slip observed in those slip systems is minimal.

The results of this investigation demonstrate the predictability and accuracy of the proposed 3D numerical framework in studying the deformation and failure of micropillars made of transformable materials. Our results illustrate that the proposed numerical approach yields

predictions in good agreement with experimental findings with respect to both mechanisms and quantitative mechanical responses. Moreover, it enables the capture of phenomena that are challenging, if not impossible, to observe solely through experimental studies. The insights provided by this work is crucial for optimizing the performance SMCs in practical applications.

CRediT authorship contribution statement

Mohsen Asle Zaeem: Writing – review & editing, Supervision, Resources, Project administration, Methodology, Investigation, Funding acquisition, Formal analysis, Conceptualization. **Amirreza Lotfolahpour:** Writing – original draft, Visualization, Validation, Software, Methodology, Investigation, Formal analysis, Data curation, Conceptualization.

Declaration of Competing Interest

The authors declare that they have no known competing financial interests or personal relationships that could have appeared to influence the work reported in this paper.

Acknowledgement

This work was supported by the U.S. National Science Foundation, under Award number CMMI 2054274. The authors are grateful for the supercomputing time allocation provided by the NSF's ACCESS (Advanced Cyberinfrastructure Coordination Ecosystem: Services & Support), Award No. DMR140008.

Appendix A

Eqs. A1 through A4 show the derivatives of each energy term in Eq. (14) with respect to OP η_p:

$$\frac{\delta F_{\mathrm{el}}}{\delta \eta_p} = \frac{1}{2} g(\phi) \varepsilon_{ij}^{\mathrm{el}} \left(C_{ijkl}^{\mathrm{M}} - C_{ijkl}^{\mathrm{T}} \right) \varepsilon_{kl}^{\mathrm{el}} - \frac{1}{2} g(\phi) C_{ijkl}(\eta_1, \quad \eta_2, \ldots, \quad \eta_m) \varepsilon_{kl}^{00}(p) \varepsilon_{ij}^{\mathrm{el}} - \frac{1}{2} g(\phi) C_{ijkl}(\eta_1, \quad \eta_2, \ldots, \quad \eta_m) \varepsilon_{ij}^{00}(p) \varepsilon_{kl}^{\mathrm{el}}, \tag{A1}$$

$$\frac{\delta F_{\mathrm{ch}}}{\delta \eta_p} = |\Delta G| (2a\eta_p - 3b\eta_p^2 + 4c\eta_p \sum_{p=1}^{m} \eta_p^2 + nd|\eta_p|^{n-1} \mathrm{sign}(\eta_p)) \; 1 < n \ll 2, \tag{A2}$$

$$\frac{\delta F_{\mathrm{gd}}}{\delta \eta_p} = \quad -B\nabla^2 \eta_p, \tag{A3}$$

$$\frac{\delta F_{\mathrm{fr}}}{\delta \eta_p} = \quad 0. \tag{A4}$$

Eqs. A5 through A8 show the derivatives of each energy term in Eq. (15) with respect to OP ϕ:

$$\frac{\delta F_{\mathrm{el}}}{\delta \phi} = \; -(1-\phi) C_{ijkl}(\eta_1, \quad \eta_2, \ldots, \quad \eta_m) \varepsilon_{kl}^{\mathrm{el}} \varepsilon_{ij}^{\mathrm{el}}, \tag{A5}$$

$$\frac{\delta F_{\mathrm{ch}}}{\delta \phi} = \quad 0, \tag{A6}$$

$$\frac{\delta F_{\mathrm{gd}}}{\delta \phi} = \quad 0, \tag{A7}$$

$$\frac{\delta F_{\mathrm{fr}}}{\delta \phi} = \quad G_c \left(\frac{\phi}{k} - k\nabla^2 \phi \right). \tag{A8}$$

The following tensors are the stress-free strain tensors of 12 M variants:

$$\varepsilon_{ij}^{00}(1) = \begin{bmatrix} 0.0418 & -0.0769 & 0 \\ -0.0769 & 0.0048 & 0 \\ 0 & 0 & -0.0114 \end{bmatrix} \varepsilon_{ij}^{00}(2) = \begin{bmatrix} 0.0418 & 0.0769 & 0 \\ 0.0769 & 0.0048 & 0 \\ 0 & 0 & -0.0114 \end{bmatrix}$$

$$\varepsilon_{ij}^{00}(3) = \begin{bmatrix} 0.0049 & 0 & -0.0769 \\ 0 & 0.0117 & 0 \\ -0.0769 & 0 & 0.0180 \end{bmatrix} \varepsilon_{ij}^{00}(4) = \begin{bmatrix} 0.0049 & 0 & 0.0769 \\ 0 & 0.0117 & 0 \\ 0.0769 & 0 & 0.0180 \end{bmatrix}$$

$$\varepsilon_{ij}^{00}(5) = \begin{bmatrix} 0.0117 & 0 & 0 \\ 0 & 0.0049 & -0.0760 \\ 0 & -0.0760 & 0.0180 \end{bmatrix} \varepsilon_{ij}^{00}(6) = \begin{bmatrix} 0.0117 & 0 & 0 \\ 0 & 0.0049 & 0.0760 \\ 0 & 0.0760 & 0.0180 \end{bmatrix}$$

$$\varepsilon_{ij}^{00}(7) = \begin{bmatrix} 0.0048 & -0.0769 & 0 \\ -0.0769 & 0.0418 & 0 \\ 0 & 0 & -0.0114 \end{bmatrix} \varepsilon_{ij}^{00}(8) = \begin{bmatrix} 0.0048 & 0.0769 & 0 \\ 0.0769 & 0.0418 & 0 \\ 0 & 0 & -0.0114 \end{bmatrix}$$

$$\varepsilon_{ij}^{00}(9) = \begin{bmatrix} 0.0117 & 0 & 0 \\ 0 & 0.0419 & -0.0760 \\ 0 & -0.0760 & -0.0180 \end{bmatrix} \varepsilon_{ij}^{00}(10) = \begin{bmatrix} 0.0117 & 0 & 0 \\ 0 & 0.0419 & -0.0760 \\ 0 & -0.0760 & -0.0180 \end{bmatrix}$$

$$\varepsilon_{ij}^{00}(11) = \begin{bmatrix} 0.0419 & 0 & -0.0769 \\ 0 & 0.0117 & 0 \\ -0.0769 & 0 & -0.0181 \end{bmatrix} \varepsilon_{ij}^{00}(12) = \begin{bmatrix} 0.0419 & 0 & 0.0769 \\ 0 & 0.0117 & 0 \\ 0.0769 & 0 & -0.0181 \end{bmatrix}$$

Data availability

Data will be made available on request.

References

[1] A. Lai, Z. Du, C.L. Gan, C.A. Schuh, Shape memory and superelastic ceramics at small scales, Science 341 (6153) (2013) 1505–1508.
[2] Z. Du, X.M. Zeng, Q. Liu, C.A. Schuh, C.L. Gan, Superelasticity in micro-scale shape memory ceramic particles, Acta Mater. 123 (2017) 255–263.
[3] X.M. Zeng, A. Lai, C.L. Gan, C.A. Schuh, Crystal orientation dependence of the stress-induced martensitic transformation in zirconia-based shape memory ceramics, Acta Mater. 116 (2016) 124–135.
[4] N. Zhang, M. Asle Zaeem, Competing mechanisms between dislocation and phase transformation in plastic deformation of single crystalline yttria-stabilized tetragonal zirconia nanopillars, Acta Mater. 120 (2016) 337–347.
[5] N. Zhang, M. Asle Zaeem, Role of grain boundaries in determining strength and plastic deformation of yttria-stabilized tetragonal zirconia bicrystals, J. Mater. Sci. 53 (8) (2018) 5706–5718.
[6] N. Zhang, M. Asle Zaeem, Effects of twin boundaries and pre-existing defects on mechanical properties and deformation mechanisms of yttria-stabilized tetragonal zirconia, J. Eur. Ceram. Soc. 40 (1) (2020) 108–114.
[7] N. Zhang, M.Asle Zaeem, Superelasticity and shape memory effect in zirconia nanoparticles, Extrem. Mech. Lett. 46 (2021) 101301.
[8] M. Mamivand, M. Asle Zaeem, H. El Kadiri, L.-Q. Chen, Phase field modeling of the tetragonal-to-monoclinic phase transformation in zirconia, Acta Mater. 61 (14) (2013) 5223–5235.
[9] M. Mamivand, M. Asle Zaeem, H. El Kadiri, Phase field modeling of stress-induced tetragonal-to-monoclinic transformation in zirconia and its effect on transformation toughening, Acta Mater. 64 (2014) 208–219.
[10] M. Mamivand, M. Asle Zaeem, H. El Kadiri, Shape memory effect and pseudoelasticity behavior in tetragonal zirconia polycrystals: a phase field study, Int. J. Plast. 60 (2014) 71–86.
[11] T. Zhao, J. Zhu, J. Luo, Study of crack propagation behavior in single crystalline tetragonal zirconia with the phase field method, Eng. Fract. Mech. 159 (2016) 155–173.
[12] J. Zhu, J. Luo, Study of transformation induced intergranular microcracking in tetragonal zirconia polycrystals with the phase field method, Mater. Sci. Eng.: A 701 (2017) 69–84.
[13] E. Moshkelgosha, M. Mamivand, Phase field modeling of crack propagation in shape memory ceramics–Application to zirconia, Comput. Mater. Sci. 174 (2020) 109509.
[14] E. Moshkelgosha, M. Mamivand, Concurrent modeling of martensitic transformation and crack growth in polycrystalline shape memory ceramics, Eng. Fract. Mech. 241 (2021) 107403.
[15] E. Moshkelgosha, M. Mamivand, Three-dimensional phase field modeling of fracture in shape memory ceramics, Int. J. Mech. Sci. 204 (2021) 106550.
[16] A. Lotfolahpour, W. Huber, M. Asle Zaeem, A phase-field model for interactive evolution of phase transformation and cracking in superelastic shape memory ceramics, Comput. Mater. Sci. 216 (2023) 111844.
[17] C. Cissé, M. Asle Zaeem, A phase-field model for non-isothermal phase transformation and plasticity in polycrystalline yttria-stabilized tetragonal zirconia, Acta Mater. 191 (2020) 111–123.
[18] C. Yu, G. Kang, Q. Kan, A micromechanical constitutive model for anisotropic cyclic deformation of super-elastic NiTi shape memory alloy single crystals, J. Mech. Phys. Solids 82 (2015) 97–136.
[19] X. Xie, G. Kang, Q. Kan, C. Yu, Phase-field theory based finite element simulation on thermo-mechanical cyclic deformation of polycrystalline super-elastic NiTi shape memory alloy, Comput. Mater. Sci. 184 (2020) 109899.
[20] Y. Zhang, Z. Moumni, Y. You, W. Zhang, J. Zhu, G. Anlas, Multiscale TRIP-based investigation of low-cycle fatigue of polycrystalline NiTi shape memory alloys, Int. J. Plast. 115 (2019) 307–329.
[21] A. Lotfolahpour, M. Asle Zaeem, Localized plastic strain accumulation in shape memory ceramics under cyclic loading, Int. J. Mech. Sci. 272 (2024) 109295.
[22] Y. Sun, J. Luo, J. Zhu, K. Zhou, A non-isothermal phase field study of the shape memory effect and pseudoelasticity of polycrystalline shape memory alloys, Comput. Mater. Sci. 167 (2019) 65–76.
[23] Y. Zhong, T. Zhu, Phase-field modeling of martensitic microstructure in NiTi shape memory alloys, Acta Mater. 75 (2014) 337–347.
[24] B. Xu, G. Kang, C. Yu, Q. Kan, Phase field simulation on the grain size dependent super-elasticity and shape memory effect of nanocrystalline NiTi shape memory alloys, Int. J. Eng. Sci. 156 (2020) 103373.
[25] M. Mamivand, M. Asle Zaeem, H. El Kadiri, A review on phase field modeling of martensitic phase transformation, Comput. Mater. Sci. 77 (2013) 304–311.
[26] Y. Zhang, X. Jin, T. Hsu, Thermodynamic calculation of Ms in ZrO2–CeO2–Y2O3 system, J. Eur. Ceram. Soc. 23 (5) (2003) 685–690.
[27] B. Bourdin, G.A. Francfort, J.-J. Marigo, Numerical experiments in revisited brittle fracture, J. Mech. Phys. Solids 48 (4) (2000) 797–826.
[28] M.J. Borden, C.V. Verhoosel, M.A. Scott, T.J. Hughes, C.M. Landis, A phase-field description of dynamic brittle fracture, Comput. Methods Appl. Mech. Eng. 217 (2012) 77–95.
[29] N. Nguyen-Thanh, W. Li, J. Huang, K. Zhou, Adaptive higher-order phase-field modeling of anisotropic brittle fracture in 3D polycrystalline materials, Comput. Methods Appl. Mech. Eng. 372 (2020) 113434.
[30] C. Miehe, M. Hofacker, F. Welschinger, A phase field model for rate-independent crack propagation: Robust algorithmic implementation based on operator splits, Comput. Methods Appl. Mech. Eng. 199 (45-48) (2010) 2765–2778.
[31] L.D. Landau, Collected papers of LD Landau, Pergamon1965.
[32] D. Wicht, M. Schneider, T. Böhlke, An efficient solution scheme for small-strain crystal-elasto-viscoplasticity in a dual framework, Comput. Methods Appl. Mech. Eng. 358 (2020) 112611.
[33] J. Rösler, H. Harders, M. Bäker, Mechanical behaviour of engineering materials: metals, ceramics, polymers, and composites, Springer Science & Business Media, 2007.
[34] M. Hofacker, C. Miehe, Continuum phase field modeling of dynamic fracture: variational principles and staggered FE implementation, Int. J. Fract. 178 (1) (2012) 113–129.
[35] M. Keuper, C. Berthold, K.G. Nickel, Long-time aging in 3 mol.% yttria-stabilized tetragonal zirconia polycrystals at human body temperature, Acta Biomater. 10 (2) (2014) 951–959.
[36] E. Camposilvan, M. Anglada, Size and plasticity effects in zirconia micropillars compression, Acta Mater. 103 (2016) 882–892.
[37] X.-S. Zhao, S.-L. Shang, Z.-K. Liu, J.-Y. Shen, Elastic properties of cubic, tetragonal and monoclinic ZrO2 from first-principles calculations, J. Nucl. Mater. 415 (1) (2011) 13–17.
[38] S.K. Chan, Y. Fang, M. Grimsditch, Z. Li, M.V. Nevitt, W.M. Robertson, E. S. Zouboulis, Temperature dependence of the elastic moduli of monoclinic zirconia, J. Am. Ceram. Soc. 74 (7) (1991) 1742–1744.
[39] R.H. Hannink, P.M. Kelly, B.C. Muddle, Transformation toughening in zirconia-containing ceramics, J. Am. Ceram. Soc. 83 (3) (2000) 461–487.
[40] H. Chalal, F. Abed-Meraim, Hardening effects on strain localization predictions in porous ductile materials using the bifurcation approach, Mech. Mater. 91 (2015) 152–166.
[41] N. Zhang, M. Asle Zaeem, Effects of grain orientations and pre-existing defects on mechanical properties and deformation mechanisms of polycrystalline yttria-stabilized tetragonal zirconia, Materialia 9 (2020) 100553.
[42] J. Lankford, R. Page, L. Rabenberg, Deformation mechanisms in yttria-stabilized zirconia, J. Mater. Sci. 23 (1988) 4144–4156.